SCIENCE CHINA
Technological Sciences

November 2013 Vol.56 No.11: 2721–2731
doi: 10.1007/s11431-013-5325-z

Numerical and experimental investigation on the effects of aft mixing chamber diaphragm in hybrid rocket motor

TIAN Hui, LI XinTian, YU NanJia & CAI GuoBiao*

School of Astronautics, Beihang University, Beijing 100191, China

Received April 27, 2013; accepted August 6, 2013; published online September 12, 2013

This paper focuses on the investigation of an aft mixing chamber diaphragm in a hybrid rocket motor. Both numerical and experimental researches are carried out to study its effects on the motor performances. The hybrid rocket motor with star fuel grain is utilized. The 90% hydrogen peroxide (HP) oxidizer and hydroxyl terminated polybutadiene (HTPB) based fuel are adopted as propellants. The diaphragm configuration settled in the aft mixing chamber includes four circular-holes with a uniform circumferential distribution. For both motors with and without the diaphragm, three-dimensional numerical simulations with gaseous combustions considered are carried out to study the flow field characteristics and motor performances. The comparison results show that the diaphragm can improve the mixing of the oxidizer and fuel. It has evident effect on increasing the motor efficiencies. Two firing experiments are conducted with full scale motors to investigate the effects of the diaphragm. The diaphragm used in the test is composed of a central steel framework and a closed thermal insulation layer. With the diaphragm employed, the combustion efficiency increases from 93.9% to 97.34% and the specific impulse efficiency increases from 80.77% to 87.28%, which verifies the positive effect of the diaphragm. Both numerical and experimental studies indicate that the scheme of the aft mixing chamber diaphragm proposed in the paper can improve the efficiencies of the hybrid rocket motor obviously.

hybrid rocket motor, diaphragm, numerical simulation, experimental investigation

Citation: Tian H, Li X T, Yu N J, et al. Numerical and experimental investigation on the effects of aft mixing chamber diaphragm in hybrid rocket motor. Sci China Tech Sci, 2013, 56: 2721–2731, doi: 10.1007/s11431-013-5325-z

Nomenclature

A	Arrhenius pre-exponential constant
c	molar concentration
c^*	characteristic velocity
E	activation energy
H	enthalpy
I_s	specific impulse
k	kinetic energy of turbulent fluctuation
M	molecular weight
$\dot{m}$	mass flow rate
n	normal direction
OF	oxidizer to fuel ratio
P	pressure
R	universal gas constant
r	fuel regression rate
T	temperature
t	time
V	volume
X,Y,Z	coordinate system
Y	mass fraction
ε	turbulence dissipation rate
ρ	density
λ	thermal conductivity

*Corresponding author (email: cgb@buaa.edu.cn)

© Science China Press and Springer-Verlag Berlin Heidelberg 2013

η	efficiency

Subscripts

c	combustion chamber
cg	combustion chamber gases
est	estimated
exp	experimental
f	fuel
g	combustion gas
o	oxidizer
ref	reference
s	fuel surface, resident
theo	theoretical

1 Introduction

In recent years, the hybrid rocket motor has become an attractive propulsion system in a wide range of fields, such as sounding rockets, target drones, launch boosters, and commercial manned spaceships [1−7]. It has some potential advantages including safety, low cost, throttling, and restarting characteristic. However, the intrinsic features of the hybrid rocket motor also lead to some disadvantages which need to be overcome. The oxidizer and fuel are stored separately and the combustion process of the hybrid rocket motor is diffusion controlled, which lead to the low fuel regression rate and combustion efficiency of the hybrid rocket motor. Low fuel regression rate can be made up by utilizing the fuel types with large burning areas or adding oxidizer or metal power into the fuel [8−10]. In addition, low thrust cruise vehicle is a good choice by making advantage of the low regression rate characteristic. On the other hand, low combustion efficiency mainly owes to the insufficient mixing and incomplete combustion of the propellants. Therefore, the efforts of enhancing propellant mixing may increase the combustion efficiency of hybrid rocket motor. The vortex hybrid rocket motor using a swirl oxidizer injector can enhance the resident time of the oxidizer, which increases the fuel regression rate and combustion efficiency [11−14]. In addition, diaphragm settled in the motor provides another method to improve combustion efficiency by increasing the mixing of the propellants.

Bettella conducted tests and simulations of a diaphragm in a hybrid rocket motor using N_2O and paraffin propellants [15]. The diaphragm with one circular hole was settled in the tube fuel grain. Experiments were performed with both lab scale and increased scale motors. Lab scale experiments showed that combustion efficiency was raised from 76% (without diaphragm) to 95% by using the diaphragm. On the increased scale, the combustion efficiency was raised from 80% (without diaphragm) to 94% with the addition of the diaphragm. In addition, Grosse and Bellomo et al. presented their numerical and experimental studies of the diaphragm in refs. [16, 17]. Their researches also showed that diaphragm could be used to improve the performances of paraffin based hybrid rocket motor. Kim investigated the effect of a kind of liquefying diaphragm in a lab scale hybrid rocket motor with paraffin fuel grain [18]. The diaphragm was made of 10% LDPE and 90% paraffin by weight. It was placed between the segmented tube grains. The fuel and the diaphragm are both combustible, but the regression rate of the diaphragm is significantly low. The combustible diaphragm has the advantage that no insulation consideration is needed compared with the metallic diaphragm. The tests showed that the combustion efficiency was raised to 95% with certain type of exposure diaphragm compared with 85% efficiency with no diaphragm grain.

Researches in the references indicate that the diaphragm has significant effects on improving the combustion efficiency of hybrid rocket motor. However, their investigations were mainly based on lab-scale motors with tube grains. In addition, all of the diaphragms were settled in the fuel grains. In order to produce a large thrust by the low regression rate hybrid rocket motor, fuel types with large burning surface areas are needed, such as star and wagon wheel grains. Nevertheless, the diaphragm in the fuel needs segmented grain configuration, which will increase the complexity and difficulty of the grain design. The purpose of this paper is to propose an aft mixing chamber diaphragm configuration on a large scale hybrid rocket motor with star fuel grain to study the motor performances. The motor utilizes hydrogen peroxide (HP) oxidizer and hydroxyl terminated polybutadiene (HTPB) based fuel propellants. The diaphragm with four circular-holes is set in the aft mixing chamber. Both three-dimensional numerical simulations and experimental studies are performed in two motors with and without the diaphragm to investigate its effects. The results indicate that the aft mixing chamber diaphragm proposed in the paper can improve the efficiencies of hybrid rocket motor obviously.

2 Numerical simulation

2.1 Geometry models

Three-dimensional numerical simulations are necessary for observing the flow fields of the non-axisymmetric hybrid rocket motors. The geometry models for simulations are built according to the actual sizes of the motors used in the experiments. The parameters of fuel grain and nozzle are identical for the both motors with and without the diaphragm. The main parameters of the motor are shown in Table 1. The star fuel grain with diameter of 285 mm and conical nozzle are employed in the motor. The diaphragm includes four circular-holes with a uniform circumferential distribution. It is settled in the aft mixing chamber of the motor. The four holes confront the solid fuel but not the fuel

Table 1 Main parameters of the hybrid rocket motor

Name	Value
Fuel grain outer diameter, mm	285
Fuel grain length, mm	1000
Fuel grain star number	8
Nozzle throat diameter, mm	58
Nozzle expansion area ratio	5
Diaphragm hole diameter, mm	60
Diaphragm hole number	4

port in order to increase the disturbance effect, which is shown in Figure 1 viewing from the forward combustion chamber. Two symmetries marked with A and B are defined in Figure 1 for further discussion. Because the motor is symmetrical, only one eighth of the motor is chosen as the computational domain. The models of the two motors with and without the diaphragm are shown in Figures 2 and 3 respectively.

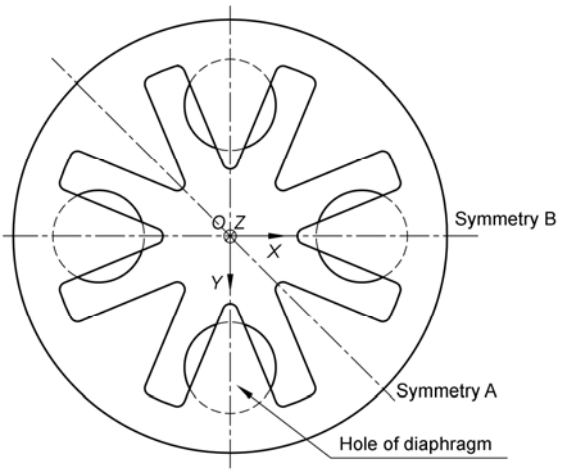

Figure 1 Schematic diagram of the fuel and diaphragm.

Figure 2 Computational domain of the motor without diaphragm.

Figure 3 Computational domain of the motor with diaphragm.

The quality of the mesh plays a dominate role in the accuracy of the simulation result. For a three-dimensional case, structured hexahedral mesh has the advantages of good orthogonality and low mesh quantity, but it is difficult to handle complicated geometries. On the contrary, unstructured tetrahedral mesh has good adaptability for complex geometries but with poor orthogonality, and larger quantity of mesh is required. A multi-block mesh scheme is adopted, and the meshes of the two motors are shown in Figures 4 and 5. For the motor without the diaphragm, the purely structured hexahedral meshes with a total number of 515662 cells are selected for the entire domain. The motor with the diaphragm mainly utilizes the hexahedral meshes, and few tetrahedral meshes are used in a small block containing the diaphragm and two thin transitional parts by the two sides of it. The total number of cells is 449591. The meshes are refined near the fuel surfaces and walls to meet the requirement of the turbulence model for the numerical simulation.

2.2 Numerical models

Three-dimensional numerical models are established with fluid dynamics, turbulence, solid fuel pyrolysis and gas phase combustions. The propellant combination in the simulation is 90% HP oxidizer and HTPB fuel. In order to simplify the simulation process, the oxidizer is assumed to be decomposed to gaseous oxygen and water vapor before spraying into the combustion chamber. The atomization and vaporization processes are neglected. The pure HPTB fuel is adopted in the simulation, which is different from the metalized HPTB used in the experiment with additives of aluminum, magnesium and carbon black. This is due to the complicated combustion process of metal power involving two-phase flow phenomenon, which increases the complexity of the simulation and requires more computational resources especially for a three-dimensional case.

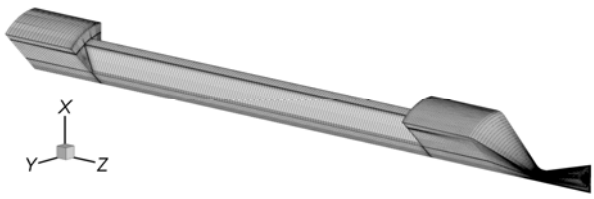

Figure 4 Meshes of the motor without diaphragm.

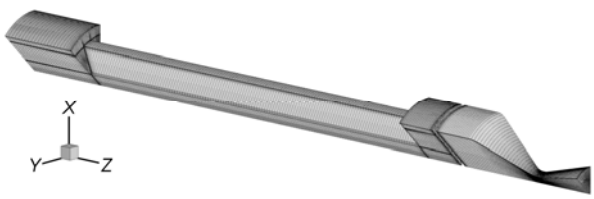

Figure 5 Meshes of the motor with diaphragm.

The governing equations involve Navier-Stokes equations, turbulence, and species transport [19]. The turbulence model adopted is realizable $k-\varepsilon$ model, which has been found to be better than the standard $k-\varepsilon$ model in the channel and boundary layer flows [20]. The simulation model treats 1,3-butadiene (C_4H_6) as the main product of HTPB pyrolysis [21], and the rate of pyrolysis is descried by Arrhenius law [22].

$$r = AT^{-E/(RT_s)}, \tag{1}$$

where T_s is the fuel surface temperature, E is the activation energy, and A is a pre-exponential reaction constant.

A global two-step reaction combustion model is used for the gaseous phase [23]. The eddy-dissipation model is chosen to control the reaction rates. It is suitable for non-premixed combustion controlled by large-eddy mixing time [24].

$$C_4H_6+3.5O_2 \longrightarrow 4CO+3H_2O \tag{2}$$

$$CO+0.5O_2 \longleftrightarrow CO_2 \tag{3}$$

The interactions between the gaseous phase and solid fuel are introduced by boundary conditions. The energy transformations at the fuel surface include convective and radiative heat flux from the flame, heat conducting into the solid fuel, and total enthalpy variation of pyrolyzing and temperature increasing. The energy conservation equation can be expressed as follows [7]:

$$-\lambda_g\left(\frac{\partial T}{\partial n}\right)_g = \rho_f r\left(H_{C_4H_6}^{T_s} - H_{HTPB}^{T_{ref}}\right). \tag{4}$$

Combining the Arrhenius law mentioned before, the fuel regression rate r and fuel surface temperature T_s can be obtained. Then the corresponding source terms of mass, momentum, energy and species can be calculated in the simulation process.

2.3 Results and discussion

In order to compare the simulation results, the initial and boundary conditions of the two motors with and without the diaphragm are identical. The oxidizer mass flow rate is 2.0 kg s^{-1}. The oxidizer inlet is set to be a mixture of 42.35% gaseous oxygen and 57.65% water vapor with temperature of 1000 K, which is about the adiabatic decomposition temperature of 90% HP. While, the fuel regression rate and fuel mass flow rate are calculated in the iteration process of the simulation. The boundary conditions of the nozzle outlet are extrapolated from the inner domain under supersonic condition.

2.3.1 Flow field characteristics

Temperature contours of the motor can reveal the flame structure and indicate the completeness of the combustion, which may affect the performances of the motor. Figures 6 and 7 give the temperature contours of main cross sections of the two motors with and without the diaphragm respectively. The maximum temperature peaks of the two motors are similar and the flame distributions of them in the fuel ports are alike. However, the temperature distributions in aft mixing chamber and nozzle are obviously different for the disturbance of the diaphragm.

Figures 8–11 present the temperature contour comparison of the two motors in the sections of front diaphragm, back diaphragm, nozzle entrance, and nozzle throat respectively. For the motor without diaphragm, the temperature is non-uniform and the flame layers of all the sections are similar to the fuel port outline. In the central core oxidizer flow, the temperature is much lower. While for the motor with diaphragm, the flow field is disturbed by the diaphragm. In the front of the diaphragm, the combustion gases are conducted to the holes and high temperature regions are formed around them. When the gas stream has passed through the diaphragm, temperatures of the most areas rise to a high level except for the regions around the holes. With the further mixing of the oxidizer and fuel in aft mixing chamber, the temperature in the nozzle becomes much higher. The temperature distribution of the nozzle throat section is almost uniform, which indicates that the heat transfers to the wall and erosions of the throat are similar in different circumferential locations. However, the flame layer of the throat section in the motor without diaphragm is still star like. Temperature gradient and convective heat transfer to the wall of throat will vary with different circumferential locations.

The combustion of the hybrid rocket motor can be classified as diffusion controlled because of the separate storage of the oxidizer and fuel. The reaction rate is mainly governed by the propellants mixing time. Therefore, the distributions of streamlines, species concentrations and oxidizer to fuel ratios are the main factors reflecting the combustion characteristics. Figures 12 and 13 show the streamlines of symmetries A and B which are defined in Figure 1. Figures 14 and 15 give the mole fraction contours of O_2. Figure 16 presents the mole fraction comparison of C_4H_6 in the nozzle entrances of the two motors and Figure 17 gives that of O_2.

Figure 12 reveals that vortexes are formed in the aft mixing chamber, which may increase the mixing of the combustion products and fuel pyrolysis. However, the oxidizer in the central flow cannot mix with the fuel sufficiently and spurts out from the nozzle directly, as seen in Figure 14. The insufficient combustion of the propellants is the main reason of the low combustion efficiency of hybrid rocket motor. With the diaphragm employed, the central oxidizer flow is conducted to the holes of the diaphragm and the mixing of the oxidizer and fuel is enhanced. Large area vortexes on both front and back sides of the diaphragm can be seen in Figure 13. As shown in Figure 15, the oxidizer is almost consumed after the diaphragm. According to

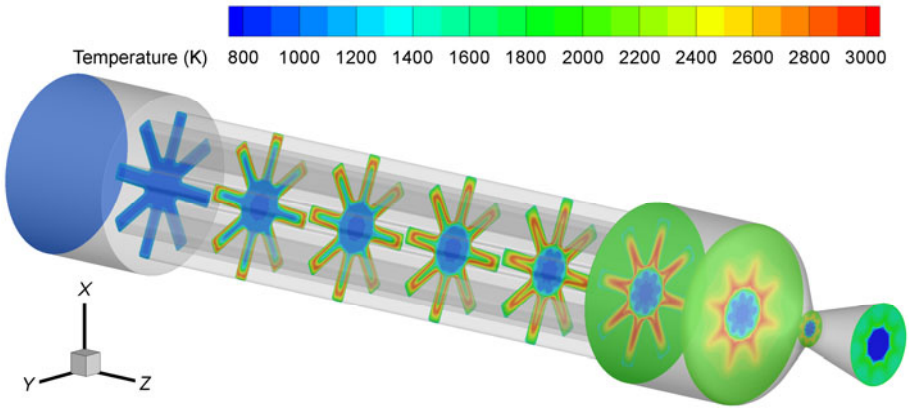

Figure 6 Temperature contours of the motor without diaphragm.

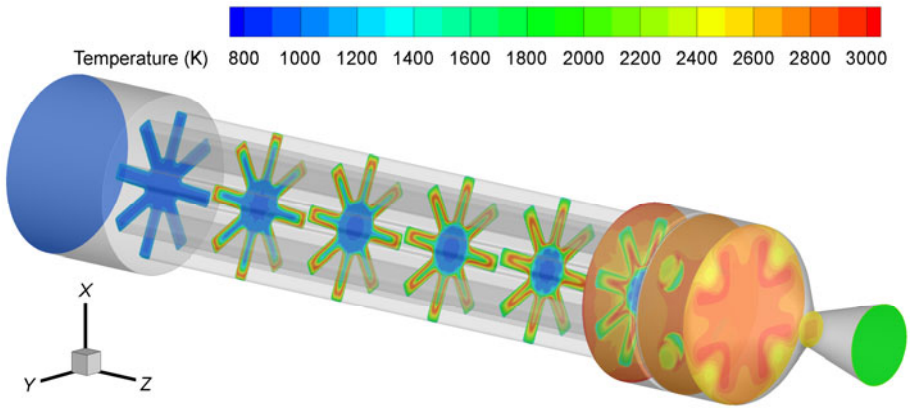

Figure 7 Temperature contours of the motor with diaphragm.

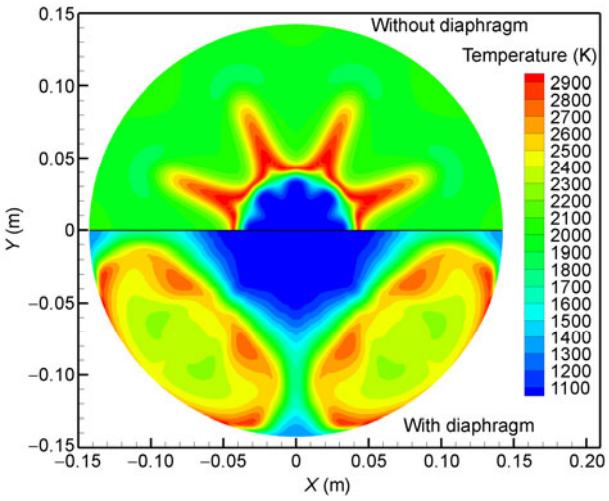

Figure 8 Temperature comparison at the front section of the diaphragm.

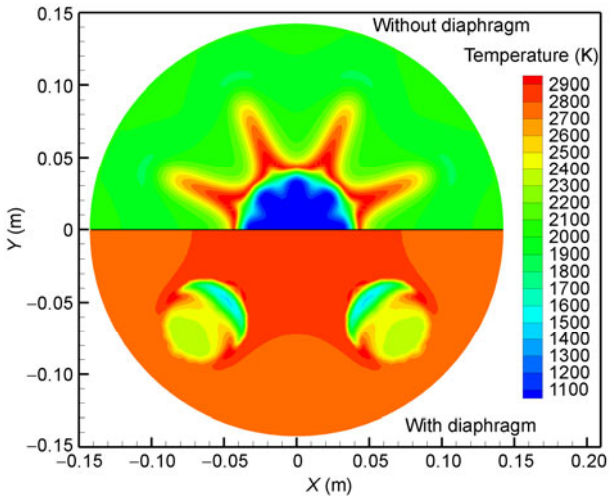

Figure 9 Temperature comparison at the back section of the diaphragm.

Figures 16 and 17, the mole fractions of C_4H_6 and O_2 are much higher when no diaphragm is used in the cross section of nozzle entrance compared with the case with diaphragm, which indicates the positive effect of the diaphragm on the combustion completeness and efficiency.

The oxidizer to fuel ratio reflects the mixing of the reactants and indicates the possibility of complete combustion. Because the oxidizer HP is assumed to be decomposed to O_2 and H_2O completely, the oxidizer to fuel ratio can be defined as the mass fraction ratio of O_2 to C_4H_6. From the

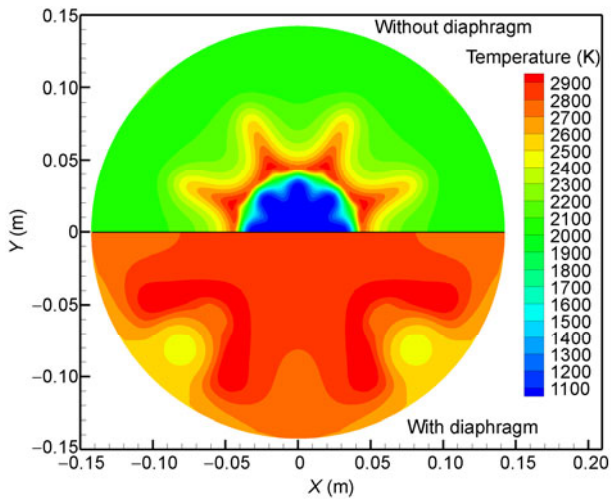

Figure 10 Temperature comparison of the nozzle entrance.

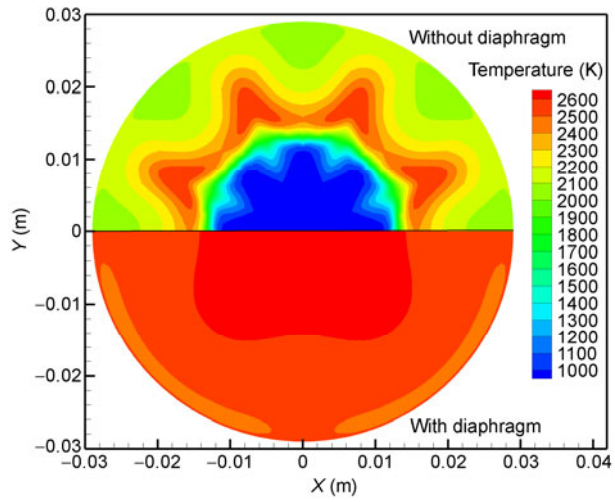

Figure 11 Temperature comparison of the nozzle throat.

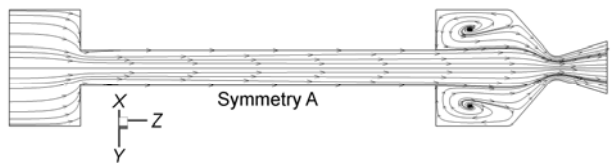

Figure 12 Streamlines in the motor without diaphragm.

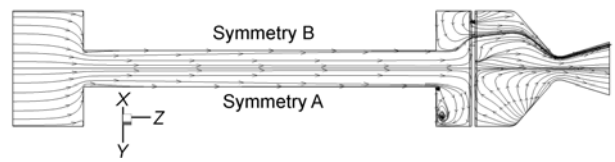

Figure 13 Streamlines in the motor with diaphragm.

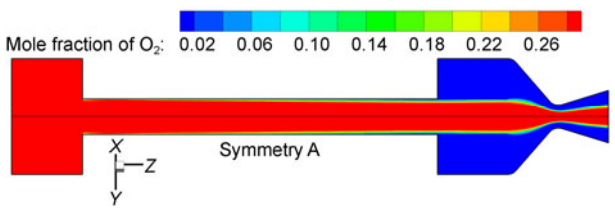

Figure 14 Mole fraction of O_2 in the motor without diaphragm.

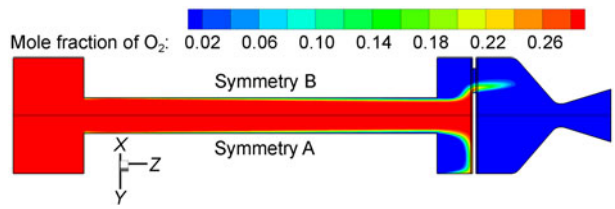

Figure 15 Mole fraction of O_2 in the motor with diaphragm.

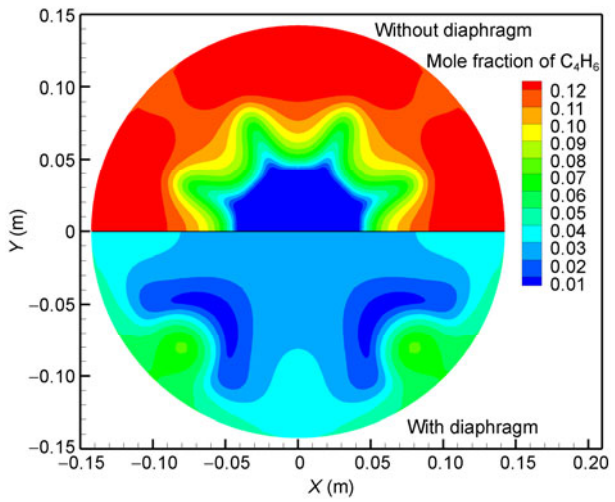

Figure 16 Mole fraction comparison of C_4H_6 in the nozzle entrance.

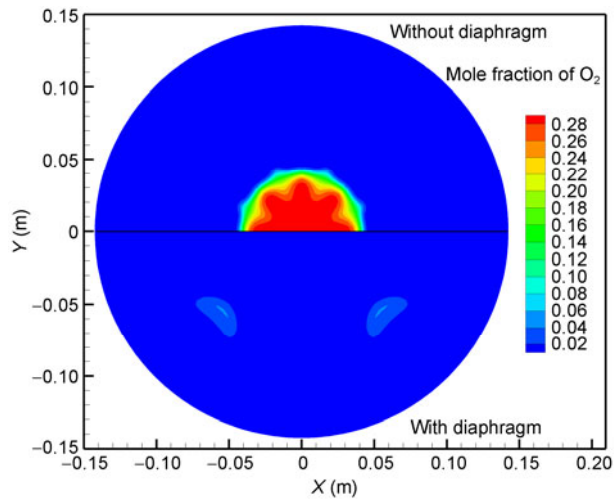

Figure 17 Mole fraction comparison of O_2 in the nozzle entrance.

stoichiometric coefficients of the two-step reaction equations, the molar concentrations of O_2 and C_4H_6 before combustion can be calculated. Then we can get the estimated oxidizer to fuel ratio before combustion.

$$OF_{\text{est}} = \frac{\left(c_{O_2} + \frac{3.5}{4}c_{CO} + \frac{5.5}{4}c_{CO_2}\right)M_{O_2}}{\left(c_{C_4H_6} + \frac{1}{4}c_{CO} + \frac{1}{4}c_{CO_2}\right)M_{C_4H_6}}. \quad (5)$$

Figure 18 gives the estimated oxidizer to fuel ratio comparison in the nozzle entrance before combustion. For the motor without diaphragm, the oxidizer to fuel ratio is extremely high even exceeding 100 in the center, yet it is lower than 1 in the surrounding area. This indicates a poor mixing of the oxidizer and fuel. With the diaphragm employed, the estimated oxidizer to fuel ratio ranges from 1.25 to 3.42 in the entire section, which is close to the optimal oxidizer to fuel ratio 2.1 of the O_2 and C_4H_6 combination. It suggests that the oxidizer and fuel are mixed well with each other and sufficient combustion is possible.

The resident time of the combustion gas can be expressed by

$$t_s = \frac{m_{cg}}{\dot{m}_o + \dot{m}_f} = \frac{V_c \rho_g}{\dot{m}_o + \dot{m}_f}, \quad (6)$$

where m_{cg} is the mass of the gases in the combustion chamber.

Sufficient resident time can provide enough time for the combustion. For the motor without diaphragm, t_s=49.6 ms; with the diaphragm employed, t_s=56.1 ms. The diaphragm increases the resident time slightly. Since the hybrid rocket motor has large combustion chamber volume, the resident time of the hybrid rocket motor is much larger than that of the liquid rocket engine, which is about 1 to 3 μs. Thus the reaction time of the both motors with and without the diaphragm is considered to be sufficient. The reaction rate of the hybrid rocket motor is mainly governed by the diffusion time. The primary effect of the diaphragm is to enhance the mixing of the oxidizer and fuel.

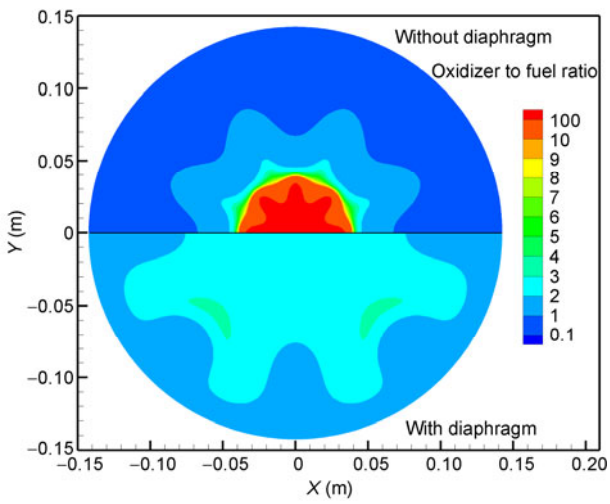

Figure 18 Oxidizer to fuel ratio comparison in the nozzle entrance.

2.3.2 *Motor performances comparison*

According to the results of simulation flow fields, the main performances of the motors can be obtained, which can be seen in Table 2. Because the flow field in the fuel port is hardly affected by the diaphragm as shown before, the average fuel regression rates of the two motors are close. Therefore, the oxidizer to fuel ratios of the two motors are almost the same under identical initial simulation conditions. The average combustion chamber pressures and thrusts of the motors can be acquired by the integration of the flow fields. The results indicate that both the combustion chamber pressure and thrust of the motor with diaphragm are higher than those without diaphragm. Combining the propellant mass flow rate and nozzle throat area, the characteristic velocity and specific impulse can be obtained. Then, the combustion efficiency and specific impulse efficiency can be acquired based on the theoretical motor performances calculated by NASA CEA code. The results in Table 2 indicate that with the diaphragm employed, the combustion efficiency rises from 82.6% to 97.8% and the specific impulse efficiency rises from 79.7% to 93.9%. It shows that the aft mixing chamber diaphragm can improve the performances of the motor obviously.

3 Experimental investigation

3.1 Experimental setup

Experimental studies of the full scale motors with the simulations are carried out to investigate the motor performances. The ground experimental system involves oxidizer feeding system, experiment platform, measurement and control system, motor assembly and so on. The oxidizer feeding system uses nitrogen as the pressure gas. The oxidizer mass flow rate is controlled by the venturi tube. The measurement system adopts National Instruments devices to acquire the pressure and thrust data. Programmable Logic Controller (PLC) is selected to control the igniter and valves in the test.

Table 2 Motor performances of the simulation results

Parameters	Without diaphragm	With diaphragm
$\dot{m}_o$[kg s^{-1}]	2.0	2.0
OF	4.58	4.58
c^* [m s^{-1}]	1296.1	1535.1
I_s [m s^{-1}]	2051.1	2417.7
η_{c^*} [%]	82.62	97.84
η_{I_s} [%]	79.67	93.90

Figure 19 gives the motor with the diaphragm on the experiment platform.

Figure 20 shows the scheme of the motor configuration with diaphragm. The parameters of the fuel grain, diaphragm configuration, and nozzle of the motor are all identical with the simulation model. The diaphragm is composed of a central steel framework and a closed thermal insulation layer made of Ethylene-Propylene-Diene Monomer (EPDM) rubber. The EPDM rubber can protect the steel framework from the high temperature combustion gases. The propellant combination used is 90% HP oxidizer and HTPB based fuel. In order to increase the density and mechanical properties, the metalized fuel is utilized with the composition of 60%HTPB+28%Al+10%Mg+2%C, which is different from the simulation one. The oxidizer mass flow rates of the both motors are 2.0 kg s^{-1}, which are identical with the simulation cases. The working time of the test for the motor without diaphragm is 30 s. However, considering that heavy erosion of the diaphragm may exist during a long working time, the test time of the motor with the diaphragm was 10 s.

3.2 Results analysis

3.2.1 Motor components

Tests of both motors with and without the diaphragm are carried out. Figure 21 shows the exhaust plume in the test when the diaphragm is employed. The working process of the test is steady. Figure 22 presents the fuel grains before and after experiments. As shown in the figure, the fuel grains have good integrity after tests. However, the fuel consumed in the motor without diaphragm is more for the long duration time of the test.

Figure 23 illustrates the diaphragm before and after the experiment. The configuration of the diaphragm is integrated, yet the erosions of the two sides are different. The erosion of the central zone on the front side of the diaphragm is the most evident due to the oxidizer-rich environment and high normal velocity flow field, which can be seen in the simulation results. On the back side, the diaphragm mainly contacts with the vortex combustion gases with a lower normal velocity. In addition, the oxidizer is consumed further which provides a more neutral environment. As a result,

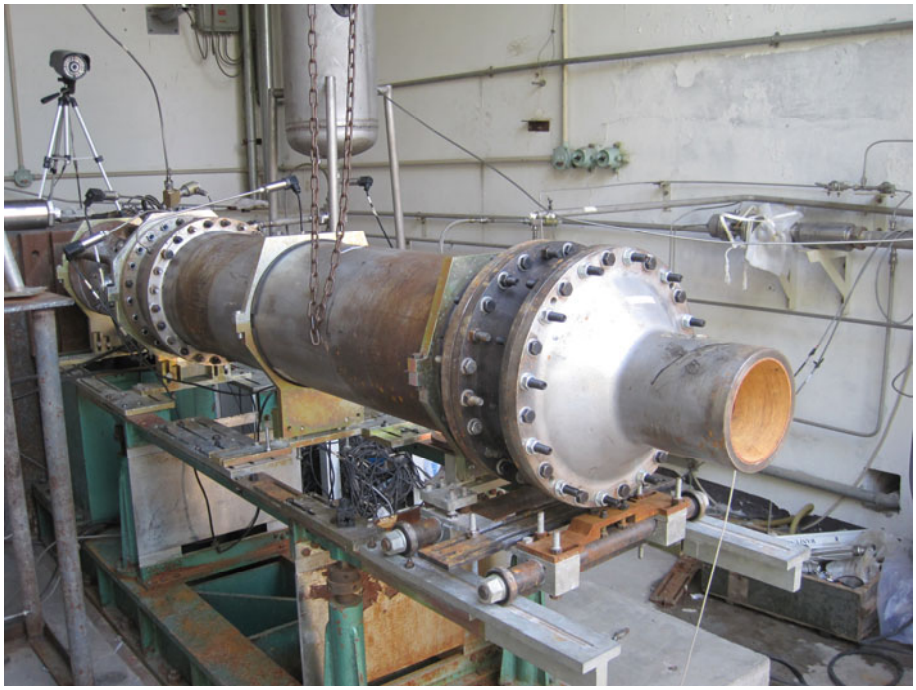

Figure 19 Photo of the hybrid rocket motor in the test platform.

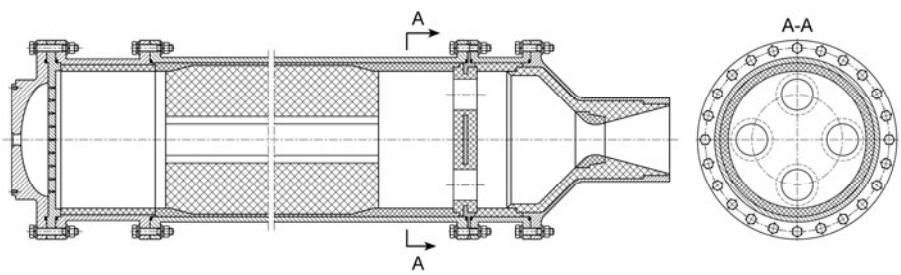

Figure 20 Scheme of the motor configuration with diaphragm.

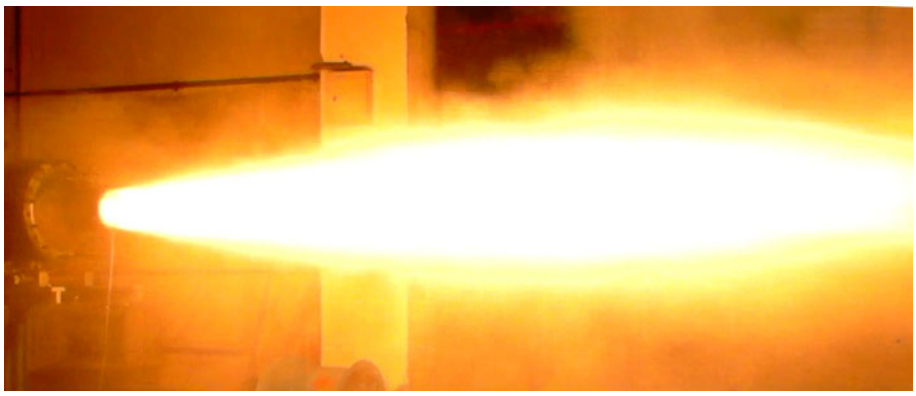

Figure 21 Exhaust plume of the motor with diaphragm.

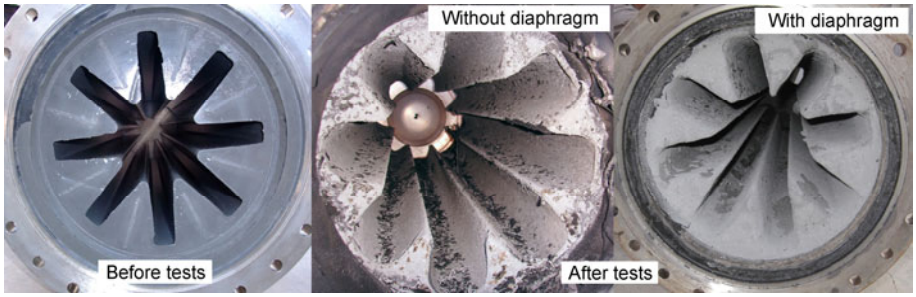

Figure 22 Fuel grains before and after tests.

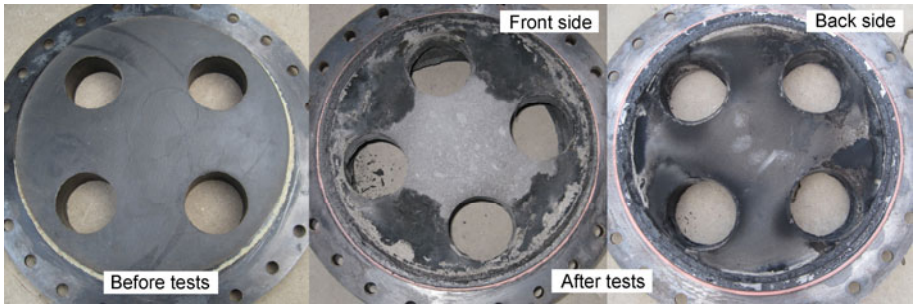

Figure 23 Diaphragm before and after tests.

the erosion of the back side is not so obvious.

Figure 24 shows the nozzle throats of the motors before and after the tests. The thermal insulation layer is made of silica phenolic and the throat lining material is graphite. For the motor without diaphragm, the throat of the nozzle after the test is no longer circular but presents star-shaped profile, which is similar to the simulation flame layer in Figure 11, due to non-uniform heat transfers and erosions. However, with the diaphragm employed, the nozzle throat after the test is still circular and the erosions of the throat at different circumferential locations are almost uniform, which matches well with Figure 11 and discussion of the simulation results. The average nozzle throat diameter of the motor without the diaphragm increases from 58 mm to 63.15 mm during the test with an erosion rate of 0.086 mm s^{-1}. However, the throat diameter change of the motor with diaphragm is not evident. The diameter of the nozzle throat is almost the same as the initial one. Firstly, it relates with the different duration time of the two tests. Besides, the non-uniform and low temperature characteristics of the nozzle throat in the motor without diaphragm may increase the metallic oxide and other condensed species, which will enhance the erosion of the nozzle throat.

3.2.2 *Efficiency analysis*

Figure 25 illustrates the chamber pressures and thrusts of the two experiments. The experimental curves are stable and no significant instabilities are noted. The combustion chamber pressure peak in the tailoff of the motor with the diaphragm is due to the higher purging gas pressure. Both the combustion chamber pressure and thrust of the motor with diaphragm are higher than ones without diaphragm under the same oxidizer mass flow rate and fuel configuration, which demonstrates the positive effects of the diaphragm on

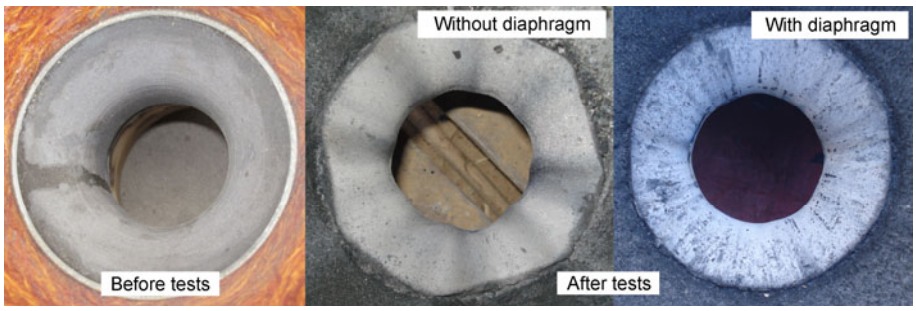

Figure 24 Nozzle throats before and after tests.

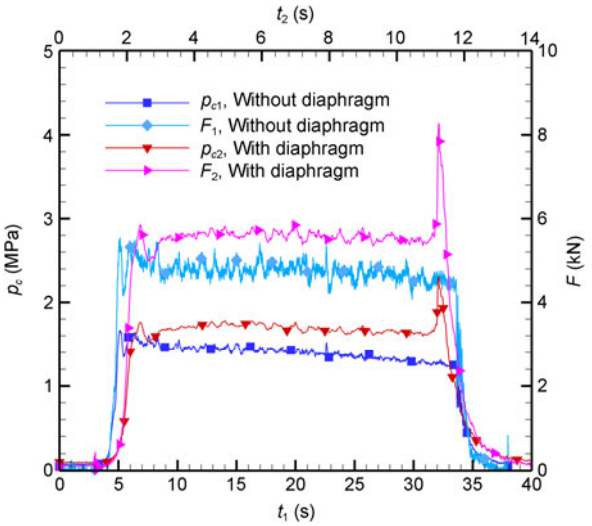

Figure 25 Experimental curves of the two motors.

the motor performances.

According to the pressure before cavitating venturi tube and the discharge coefficient obtained from the cold flow experiments, the oxidizer mass flow rates in the tests can be calculated. The theoretical characteristic velocity and specific impulse under the given combustion chamber pressure and oxidizer to fuel ratio are acquired based on NASA CEA code. Combined with the fuel regression rate law and fuel masses consumed in the tests, the theoretical internal ballistics performances are calculated. Then the theoretical and experimental performances are compared with each other to analyze the motor efficiencies. The change rate of the nozzle throat diameter is assumed to be linear in the theoretical calculation. The analyses are conducted based on the burning time of the motor t_b, which starts at the 10% of the steady combustion chamber pressure and ends when the combustion chamber pressure drops to 90% of the stable value. The combustion efficiency and specific impulse efficiency are calculated with the following equations:

$$\eta_{c^*} = \frac{c^*_{\text{exp}}}{c^*_{\text{theo}}} = \frac{\int_0^{t_b} p_{\text{c_exp}} A_t \mathrm{d}t \Big/ \left(\dot{m}_{\text{o}} + \dot{m}_{\text{f}}\right)}{\int_0^{t_b} c^*_{\text{theo}} \mathrm{d}t \Big/ t_b} \approx \frac{\int_0^{t_b} p_{\text{c_exp}} \mathrm{d}t}{\int_0^{t_b} p_{\text{c_theo}} \mathrm{d}t}, \quad (7)$$

$$\eta_{I_s} = \frac{I_{s_\text{exp}}}{I_{s_\text{theo}}} = \frac{\int_0^{t_b} F_{\text{exp}} \mathrm{d}t \Big/ \left(\dot{m}_{\text{o}} + \dot{m}_{\text{f}}\right)}{\int_0^{t_b} I_{s_\text{theo}} \mathrm{d}t \Big/ t_{\text{b}}} \approx \frac{\int_0^{t_b} F_{\text{exp}} \mathrm{d}t}{\int_0^{t_b} F_{\text{theo}} \mathrm{d}t}. \quad (8)$$

Table 3 presents the main results of the experiments. With the diaphragm employed, the combustion efficiency increases from 93.90% to 97.34% and the specific impulse efficiency increases from 80.77% to 87.28%. However, the absolute values of the experimental efficiencies are different from the numerical ones. The efficiency increments of the experiments are lower than those of the simulation results. This may be due to the differences between the numerical models and experimental setups. The simulation considers only gaseous reactions and the radiative effects are neglected. Meanwhile, the fuels used in the experiments are metalized HTPB which are different from the pure one in simulations. The two-phase flow loss caused by the diaphragm is neglected in the simulation, which may enlarge the performance increments of the diaphragm. Even if some of the numerical and experimental results match well with each other, it does not indicate the precise predictions of the simulation but the assumptions and simplifications may compensate with each other. However, both numerical and experimental results indicate that the diaphragm can improve the combustion efficiency and specific impulse efficiency evidently.

Table 3 Motor performances of the experimental results

Parameters	Without diaphragm	With diaphragm
m_{o} [kg s^{-1}]	1.997	2.025
OF	3.148	2.290
t [s]	30	10
p_c [MPa]	1.401	1.690
F [N]	4.753	5.602
c^* [m s^{-1}]	1518.3	1555.4
I_s [m s^{-1}]	1779.9	1932.5
η_{c^*} [%]	93.90	97.34
η_{I_s} [%]	80.77	87.28

4 Conclusions

This paper proposes a diaphragm configuration in the aft mixing chamber of a hybrid rocket motor to improve the motor performances. The comparisons between motors with and without the diaphragm are performed. Both numerical and experimental results demonstrate the positive effects of the diaphragm. The main conclusions are as follows.

1) Three-dimensional numerical simulations of the hybrid rocket motors with and without the diaphragm are performed based on the HTPB and HP propellant combination. The fuel grain parameters and nozzle sizes of the two motors are identical. The temperature contours, streamlines, species concentrations, estimated oxidizer to fuel ratios, and combustion gas resident time of them are presented. According to the simulation results, the diaphragm disturbs the flow field in aft mixing chamber. It enhances the mixing of the oxidizer and fuel and increases the combustion gas resident time. The temperature of the nozzle in the motor with diaphragm is more uniform due to more completely mixing and sufficient combustion. The combustion efficiency and specific impulse efficiency are both increased evidently by the diaphragm configuration. The main effect of the diaphragm is to enhance the mixing of the reactants of the diffusion controlled hybrid rocket motor combustion.

2) Experimental studies are performed using full scale hybrid rocket motors with the numerical simulation ones. Both motors with and without the diaphragm are tested. The diaphragm configuration is integrated after the test and the most obvious erosion is in the central front face. With the diaphragm employed, the erosion of the nozzle throat is reduced. In addition, the erosions at different circumferential locations of the nozzle throat are more uniform. The profile of the nozzle throat is still round after experiment. These results match well with the numerical predictions. With the diaphragm used, the combustion efficiency increases from 93.9% to 97.34% and the specific impulse efficiency increases from 80.77% to 87.28%. The experimental results suggest that the diaphragm configuration proposed in this paper is an effective scheme to improve the motor performances.

1 Chiaverini M J, Kuo K K. eds. Fundamentals of hybrid rocket combustion and propulsion. Vol 28: Progress in Astronautics and Aeronautics. Reston, Virginia: AIAA, 2006

2 Dyer J, Doran E, Dunn Z, et al. Design and development of a 100 km nitrous oxide/paraffin hybrid rocket vehicle. AIAA Paper 2007-5362, 2007

3 Larsen C R. Development of guide to commercial space transportation reusable launch vehicle operations & maintenance. AIAA Paper 2005-6795, 2005

4 Taylor F W, Howard R. Dream chaser for space transportation: tourism, NASA and military integrated on a Atlas V. AIAA Paper 2008-7837, 2008

5 Rao D L, Cai G B, Zhu H, et al. Design and optimization of variable thrust hybrid rocket motors for sounding rockets. Sci China Tech Sci, 2012, 55(1): 125−135

6 Li J H, Yu N J, Zeng P, et al. Design and integrated simulation of a pressurized feed system of the dual-thrust hybrid rocket motor. Sci China Tech Sci, 2013, 56(4): 989−1000

7 Li X T, Tian H, Cai G B. Numerical analysis of fuel regression rate distribution characteristics in hybrid rocket motors with different fuel types. Sci China Tech Sci, 2013, 56(7): 1807−1817

8 Farbar E, Louwers J, Kaya T. Investigation of metallized and non-metallized hydroxyl terminated polybutadiene/hydrogen peroxide hybrid rockets. J Propul Power, 2007, 23(2): 476−486

9 George P, Krishnan S, Varkey P M, et al. Fuel regression rate in hydroxyl-terminated-polybutadiene/gaseous-oxygen hybrid rocket motors. J Propul Power, 2001, 17(1): 35−42

10 Risha G A, Ulas A, Boyer E, et al. Combustion of HTPB-Based solid fuels containing nano-sized energetic powder in a hybrid rocket motor. AIAA Paper 2001-3535, 2001

11 Jansen R, Teegarden E, Gimelshein S. Characterization of a vortex-flow end-burning hybrid rocket motor for nanosatellite applications. AIAA Paper 2012-0125, 2012

12 Lee C, Na Y, Lee J, et al. Effect of induced swirl flow on regression rate of hybrid rocket fuel by helical grain configuration. Aerosp Sci Technol, 2007, (11): 68−76

13 Knuth W H, Chiaverini M J, Sauer J A, et al. Solid-fuel regression rate behavior of vortex hybrid rocket engines. J Propul Power, 2002, 18(3): 600−609

14 Lee C, Na Y, Lee G. The enhancement of regression rate of hybrid rocket fuel by helical grain configuration and swirl flow. AIAA Paper 2005-3906, 2005

15 Bettella A, Lazzarin M, Bellomo N, et al. Testing and CFD simulation of diaphragm hybrid rocket motors. AIAA Paper 2011-6023, 2011

16 Grosse M. Effect of a diaphragm on performance and fuel regression of a laboratory scale hybrid rocket motor using nitrous oxide and paraffin. AIAA Paper 2009-5113, 2009

17 Bellomo N, Lazzarin M, Barato F, et al. Numerical investigation of the effect of a diaphragm on the performance of a hybrid rocket motor. AIAA Paper 2010-7033, 2010

18 Kim H, Kim S, Woo K, et al. Investigation on the effect of liquefying diaphragm in hybrid rocket motors using paraffin-based fuel. AIAA Paper 2011-5824, 2011

19 Venkateswaran S, Deshpande M, Merkle C L. The Application of preconditioning to reacting flow cornputations. AIAA Paper 95-1673, 1995

20 Shih T H, Liou W W, Shabbir A, et al. A new k-ε eddy-viscosity model for high reynolds number turbulent flows—model development and validation. Computers Fluids, 1995, 24(3): 227−238, 346

21 Chiaverini M J, Harting G C, Lu Y, et al. Pyrolysis behavior of hybrid rocket solid fuels under rapid heating conditions. AIAA Paper 97-3078, 1997

22 Cohen N S, Fleming R W, Derr R L. Role of binders in solid propellant combustion. AIAA J, 1974, 12(2): 212−218

23 Venkateswaran S, Merkle C L. Size scale-up in hyrid rocket motors. AIAA Paper 96-0647, 1996

24 Magnussen B F, Hjertager B H. On mathematical models of turbulent combustion with special emphasis on soot formation and combustion. Symp (Int) Combus, 1977, 16(1): 719−729